Original Article

Extended state observer–based fractional order sliding-mode control of piezoelectric actuators

Shuyou Yu[1] ⓘ**, Yangyang Feng[1] and Xiaoping Yang[2]**

Abstract

Tracking control of piezoelectric actuators is considered in the article. A Hammerstein model is used to depict the rate-dependent hysteresis characteristics of piezoelectric actuators, in which a Bouc–Wen model is to describe the static hysteresis characteristic, and a linear time-invariant system is to describe its rate-dependent characteristics. An inverse Bouc–Wen model connected in series with the piezoelectric actuator is used to compensate the static hysteresis nonlinearity of piezoelectric actuators. Furthermore, an extended state observer–based fractional order sliding-mode control is designed to deal with higher order unmodelled dynamics and inverse compensation errors. Moreover, the bounds of the estimation error of the extended state observer are estimated, and the convergence of the proposed control strategy is proved. Experimental results show that the proposed scheme can track both single and composite input signals within a certain frequency range. Compared with extended state observer–based conventional sliding-mode controller, the proposed scheme has faster response time and smaller tracking error.

Introduction

Piezoelectric actuators (PEAs) uses the piezoelectric material to produce the inverse piezoelectric effect and the electrostriction effect. Since the PEA has many great characteristics such as small size, high precision, high resolution, and fast frequency response, it has become an important driving element in the precise position system. PEA is widely used in the scanning probe microscope,[1] active optical element,[2] vibration control,[3] biomedical engineering,[4] and so on.

The hysteresis characteristics are the multi-valued nonlinear phenomenon between the applied voltage and the output displacement of the PEA, which are rate-dependent, that is, strongly depending on frequency of the input voltage. This rate-dependent hysteresis behavior seriously affects the control accuracy of the system and makes the system closed-loop unstable.[5]

Both physical and phenomenological models are used to describe hysteresis nonlinearities. The existing physical models of the PEA are Maxwell model,[6] Duhem hysteresis model,[7] Jiles Atherton model,[8] and so forth. Maxwell model is a lumped parameter model.[6]

The criteria and methods for solving the parameters of Maxwell model are provided by Qin and Hu.[9] Compared with Maxwell model, Duhem hysteresis model[7] has more parameters which are difficult to be determined in general. In some sense, Jiles Atherton model[8] is too complex to identify the parameters. Preisach model,[10] Prandtl–Ishlinskii model,[11] Bouc–Wen model,[12,13] artificial neural network model,[14] and support vector machine model[15] are phenomenological models. Preisach model[10] requires a large amount of experimental data to identify parameters, since Preisach model contains double integrals. Prandtl–Ishlinskii model,[11] compared with the Preisach model, possesses the easy-to-use property for construction and identification. Controller design

[1]Department of Control Science and Engineering, Jilin University, Changchun, China
[2]Department of Electronic Engineering, Jilin University, Changchun, China

Corresponding author:
Shuyou Yu, Department of Control Science and Engineering, Jilin University, Changchun 130012, China.
Email: shuyou@jlu.edu.cn

with Bouc–Wen model is much easier[12,13] since it contains fewer parameters. The particle swarm optimization (PSO) algorithm and genetic algorithm are used to identify the Bouc–Wen model.[12,13] Note that the parameters of the phenomenological model of hysteresis systems are only related to data of the input and the output.

An intuitive scheme to deal with the hysteresis nonlinearity is to construct an inverse model to compensate it directly.[16] Furthermore, in order to reduce the influence of compensation errors and model-plant mismatches, it is necessary to adopt a feedback control law. Proportional–integral–derivative (PID) control is used as a feedback controller that neither inverse compensation errors nor disturbances are considered in the process of controller design.[17] The inverse compensation error or modeling error is regarded as model uncertainties, and an $\mathcal{H}_\infty$ robust controller is designed to reduce the influence of uncertainties and to ensure the robust stability.[18,19] Sliding-mode control (SMC) can effectively deal with model uncertainties and disturbances of nonlinear systems.[20] Some effort has been made to achieve better performance, for example, fuzzy SMC can adapt the input saturation and the matched uncertainty with unknown upper bounds,[21–23] the terminal SMC guarantees that the tracking error approaches 0 in a finite time.[24] Compared with traditional calculus, the fractional calculus operator has faster convergence speed and memory characteristics. Fractional order sliding-mode controller[25–28] can achieve good tracking performance, robustness to external disturbances or model uncertainties, and finite-time convergence to the desired trajectory. In SMC design, the upper bound of disturbances or model uncertainties need to be acquired in the control design, although it is difficult in general. In order to overcome this deficiency, SMC with disturbance estimation is proposed,[29–33] in which the upper bound of disturbances or model uncertainties is no longer needed. The existing SMC with disturbance estimation featured with a conventional SMC or a simple disturbance estimation strategy produces a slow response speed and insufficient estimation of disturbances. In the article, a fractional order SMC with extended state observer is applied to deal with the hysteresis nonlinearity of PEAs. Fractional order operators can achieve fast response and small tracking error, and the extended state observer can achieve high-precision estimation of disturbances and unmeasured states.

Recently, some schemes without hysteresis inverse models are put forward, for example, both smith predictor[34] and hysteresis observer[35,36] are designed to compensate the hysteresis nonlinearity of PEAs. Although the control scheme without hysteretic inverse models can avoid the heavy computational burden caused by the hysteretic inverse model, the design of controller highly relies on the hysteresis model and is difficult to guarantee stability.

In this article, the hysteresis characteristic of PEAs is described by a Hammerstein model, in which the static

hysteresis nonlinearity is represented by a Bouc–Wen model and its parameters are identified by PSO algorithm. A second-order linear time-invariant system is to capture rate-dependent characteristics, and its parameters are identified with nonlinear least squares by system identification toolbox of Matlab. In the controller design section, an inverse Bouc–Wen model is connected in series to the PEA in order to compensate the static hysteresis of PEAs. An extended state observer–based fractional order sliding-mode control (ESO-FOSMC) is designed, in which the extended state observer is used to observe and compensate the high-order unmodelled dynamics, compensation errors and external disturbances. Fractional order SMC is used to achieve fast response and to minimize tracking errors. Moreover, the bounds of the estimation error of the extended state observer are estimated and the convergence stability of the proposed control strategy is proved, respectively. The experimental results show the effectiveness of the proposed strategy. Compared with an extended state observer–based conventional sliding-mode controller (ESO-SMC), the design ESO-FOSMC method has faster response time and smaller tracking error.

Rate-dependent Hammerstein model of PEA

Rate-dependent hysteresis system is referred to the system, whose output is related to not only the current and the historical input signal but also the variable rate of the current and historical input signal. PEAs represent this rate-dependent characteristic, that is, the output of the PEA is relevant to the change of input voltage frequency, as shown in Figure 1.

The Hammerstein model is a block-connected nonlinear model consisting of a static nonlinear function
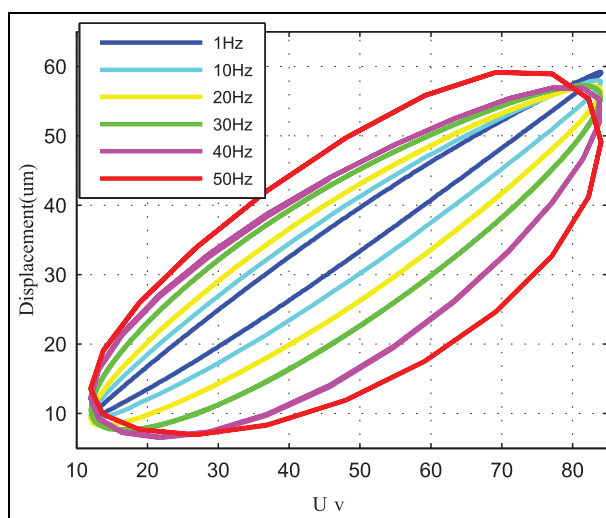

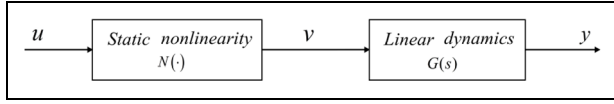**Figure 1.** The rate-dependent hysteresis characteristics of PEA.
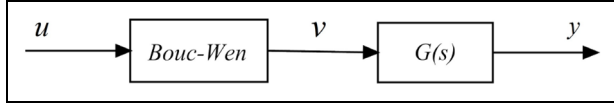
Figure 2. The structure of Hammerstein model.

Figure 3. The structure of Hammerstein model of PEA.

followed by a linear dynamic system[37,38] which is shown in Figure 2.

The experiment indicates that the shape of the hysteresis loop is almost unchanged when the PEA is working over its low-frequency range. There is a rate-dependent characteristic of the PEA at higher frequencies. In this article, the Hammerstein model is used to describe the rate-dependent characteristics of PEAs. The static nonlinear part of the Hammerstein model is described by the Bouc–Wen model, and the linear dynamic is a second-order linear time-invariant system. The rate-dependent hysteresis model of the PEA is shown in Figure 3.

Bouc–Wen model

Compared with other models, Bouc–Wen model contains fewer parameters which can be identified with fewer data. Thus, Bouc–Wen model is adopted in this article. The Bouc–Wen model describes the size and shape of the hysteresis loop through a nonlinear equation with uncertain parameters. By choosing the parameters of the equation reasonably, a large number of hysteresis loops with different shapes can be obtained to simulate the hysteresis characteristics of the actual object. The mathematical expression of Bouc–Wen model is

$$v = du - h$$
$$\dot{h} = \alpha d\dot{u} - \beta|\dot{u}||\dot{u}|^{n-1}h - \gamma\dot{u}|h|^n \tag{1}$$

where u is the input voltage, v is the system output (hysteresis displacement), h represents the hysteresis term, and d is the proportional gain. The magnitude of the hysteresis loop is determined by α, and the shape of hysteresis loop is determined by β and γ. Although the model order n has no significant effect on the hysteresis shape, it mainly determines the smoothness of the hysteresis curve.

Linear dynamic model

The Hammerstein model describing the rate-dependent hysteresis characteristics of PEA is established as follows

$$m\ddot{y} + c\dot{y} + ky = k_1 v \tag{2a}$$

$$\begin{cases} v = du - h \\ \dot{h} = \alpha d\dot{u} - \beta|\dot{u}|h - \gamma\dot{u}|h| \end{cases} \tag{2b}$$

where the model order of Bouc–Wen model is set to $n = 1$, y represents the output displacement of the PEA. The parameters m, c, k, d, and k_1, respectively, represent the mass, damping, stiffness, effective piezoelectric coefficients, and the platform gain of the piezoelectric system.

Linear dynamic model $G(s)$ reflects the dynamic characteristics of PEAs

$$G(s) = \frac{y(s)}{v(s)} = \frac{k_1}{ms^2 + cs + k} \tag{3}$$

Choose $x_1 = y$, $x_2 = \dot{y}$, the state-space model of the given PEA is

$$\begin{cases} \begin{bmatrix} \dot{x}_1 \\ \dot{x}_2 \end{bmatrix} = \begin{bmatrix} 0 & 1 \\ -\frac{k}{m} & -\frac{c}{m} \end{bmatrix} \begin{bmatrix} x_1 \\ x_2 \end{bmatrix} + \begin{bmatrix} 0 \\ \frac{k_1}{m} \end{bmatrix} v \\ y = \begin{bmatrix} 1 & 0 \end{bmatrix} \begin{bmatrix} x_1 \\ x_2 \end{bmatrix} \end{cases} \tag{4}$$

$$\begin{cases} \dot{h} = ad\dot{u} - \beta|\dot{u}|h - \gamma\dot{u}|h| \\ v = du - h \end{cases}$$

Parameter identification

The experiment shows that the shape of the hysteresis loop is almost unchanged when the PEA is working over its low-frequency range. Here the PSO algorithm is used to identify its parameters d, α, β, and γ of the Bouc–Wen model of PEAs according to its input and output data at some low frequencies.

The PSO algorithm is proposed by Kennedy and Eberhart[39] while they were studying the bird predator behavior. The PSO algorithm is inspired by the behavior characteristics of the biological population and is used to solve the optimization problem, in which each particle represents a potential solution of the problem and corresponds to a fitness value determined by the fitness function. The velocity of the particle determines the direction and distance of the particle movement, which is adjusted dynamically by the experience of itself and other particles so as to find a better solution accordingly.

In PSO, each particle represents a set of model parameters, and a fitness function is set to calculate the distance between the particle and the optimal one. In the process of the Bouc–Wen model parameter identification, the root mean square (RMS) error

$$J = \sqrt{\frac{1}{n_m} \sum_{i=1}^{n_m} (y_{\exp}(i) - y_{mdl}(i))^2} \tag{5}$$

is chosen as the fitness function, where $y_{\exp}(i)$ is measured displacement and $y_{mdl}(i)$ is evaluated

Table 1. PSO parameter settings.

Parameters	K	N	D	c_{1s}	c_{1f}	c_{2s}	c_{2f}	w_{max}	w_{min}
Value	2000	50	4	4	1	1	4	0.9	0.4

displacement at the ith h sampling time, n_m is the number of sampling points ($n_m = 600$). The particle velocity and position of the updated equation are

$$v_{id}(t + 1) = w(t)v_{id}(t) + c_1(t)r_1(p_{id}(t) - x_{id}(t))$$
$$+ c_2(t)r_2(p_{gd}(t) - x_{id}(t))$$
$$x_{id}(t + 1) = v_{id}(t + 1) + x_{id}(t)$$

where $x_{id} = (x_{i1}, x_{i2}, \ldots, x_{iD})$ and $v_{id} = (v_{i1}, v_{i2}, \ldots, v_{iD})$ represent the position and the velocity of a particle, respectively; $p_{id} = (p_{i1}, p_{i2}, \ldots, p_{iD})$ represents the optimal position of the current particle; $p_{gd} = (p_{g1}, p_{g2}, \ldots, p_{gD})$ represents the optimal position of group particles; N is the number of particles and $i \in [1, N]$ is an integer; D is the particle dimension; r_1 and $r_2 \in [0, 1]$ are random numbers. The cognitive parameters and social parameters $c_1(t)$ and $c_2(t)$ are

$$c_1(t) = \frac{t}{K}(c_{1s} - c_{1f}) + c_{1f} \tag{6}$$
$$c_2(t) = \frac{t}{K}(c_{2s} - c_{2f}) + c_{2f} \tag{7}$$

where c_{1s} and c_{1f} are the initial and final values of cognitive parameters; c_{2s} and c_{2f} are the initial value and final value of social parameters; t is the current iteration number and K is the maximum iteration number.

The inertia weight of $w(t)$ satisfies

$$w(t) = w_{max} - (w_{max} - w_{min}) * t/K \tag{8}$$

where w_{max} and w_{min} are the final weight and the initial weight, respectively. The parameters of PSO algorithm are listed in Table 1.

The values of parameters of the Bouc–Wen model identified by the PSO are as follows

$$d = 1.2560 \quad \alpha = 0.3438$$
$$\beta = 0.4656 \quad \gamma = 0.04474$$

The outputs of the Bouc–Wen model and the PEA are shown in Figure 4, while the input signal is

$$u_d = 12 * (2 \sin(2\pi f t) + 3)$$

with $f = 0.5$ Hz.

A set of sinusoidal sweep signals $u_d = 12 * (2 \sin(2\pi\varpi t) + 3)$ is used to stimulate the PEA stage, whose frequency of ϖ increases at a linear rate with time and varies in $0.1 - 50$ Hz. Thereafter, a set of discrete inputs $u(t)$ and outputs $y(t)$ are obtained accordingly.

According to the Bouc–Wen model identified by the PSO algorithm, the value of $v(t)$ is calculated. The linear second-order system parameters are identified with nonlinear least squares by Matlab identification toolbox
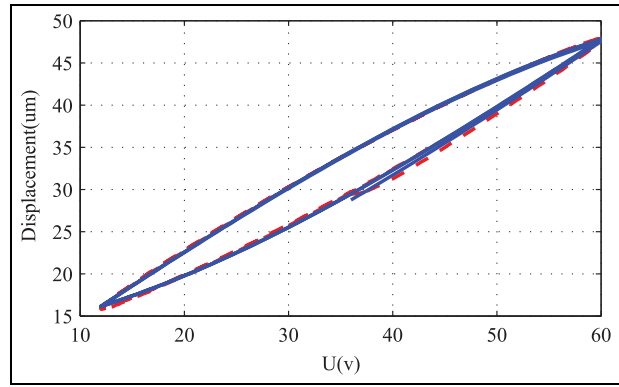

Figure 4. Outputs of PEA and Bouc–Wen mode at $f = 0.5$ Hz, solid line: the output of Bouc–Wen mode, dashed line: experimental output.

$$G(s) = \frac{546,600}{s^2 + 726.5\,s + 551,400} \tag{9}$$

Note that in the process of identification, $v(t)$ and $y(t)$ are treated as input and output sequences, respectively.

The parameter values of the linear dynamic model are identified as follows

$$m = 1\,\text{kg} \quad c = 726.5\,\text{N s/m}$$
$$k = 551,400\,\text{N/m} \quad k_1 = 546,600\,\text{N/m}$$

Model validation

Validation is to demonstrate that the model is a reasonable representation of the actual system, that is, to show the model can reproduce system behaviors with enough fidelity to satisfy analysis objectives. In order to validate the rate-dependent hysteresis model equation (4), a hardware-in-the-loop simulation system is constructed as shown in Figure 5, where the hardware in the system is the PEA and the controller is a Simulink model.

Fast prototype design is adopted in the controller design and implementation. The controller is constructed in the real-time workspace (RTW) toolkit of Simulink. The designed controller is then transformed into C-code by the C-compiler in Simulink before infixed into the Target PC. In the PEA stage, both A/D and D/A conversions are based on Advantech PCI-1710 data acquisition card, and the rated frequency range of it is about $0 - 50$ Hz.

Figures 6–8 show the comparison of hysteresis loop curves of experiments and models while the reference input is $u_d = 12 * (2 \sin(2\pi f t) + 3)$, and the frequencies of the reference signal of f are 30, 40, and 50 Hz, respectively.

Figures 9 and 10 show the comparison of hysteresis loop curves of experiments and models, while the reference input is a composite signal

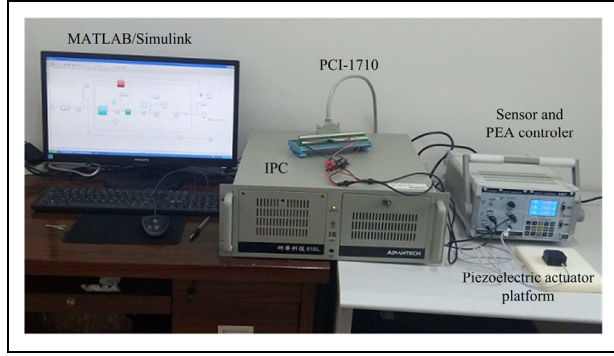$$u_d = 12 * 0.5(5 - \sin(2\pi f_1 t) - \cdots - \sin(2\pi f_5 t))$$
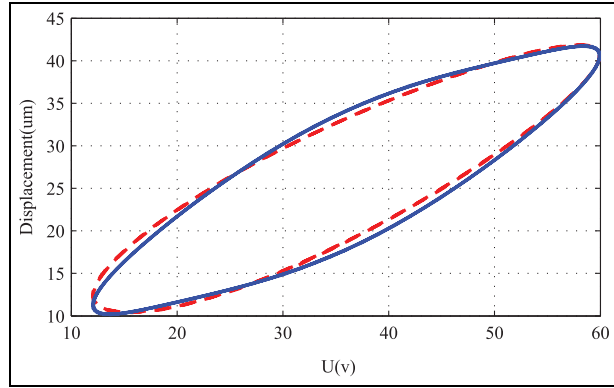
Figure 5. Piezoelectric actuators stage.

Figure 6. Model validation at f = 30 Hz, solid line: simulation output, dashed line: experimental output.
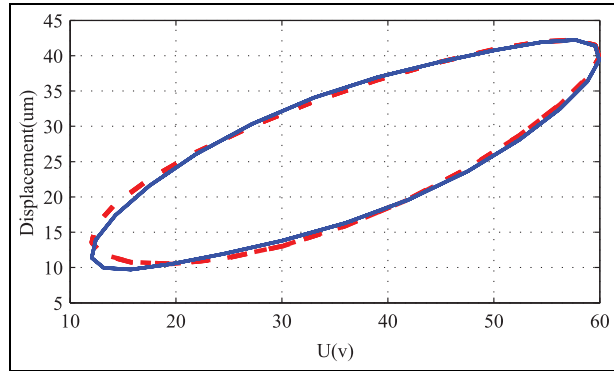

Figure 7. Model validation at f = 40 Hz, solid line: simulation output, dashed line: experimental output.

where f_1 = 10 Hz, f_2 = 20 Hz, f_3 = 30 Hz, f_4 = 40 Hz, and f_5 = 50 Hz and f_1 = 5 Hz, f_2 = 15 Hz, f_3 = 25 Hz, f_4 = 35 Hz, and f_5 = 45 Hz, respectively. The RMS error and the maximum error of the model deviation at the different frequency are listed in Table 2.

Controller design

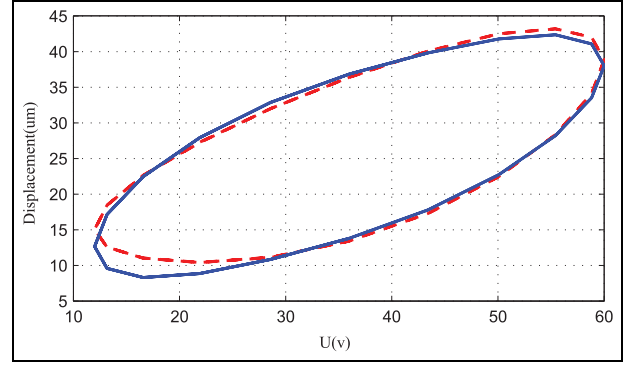The controller consists of two parts: an inverse Bouc–Wen model and an ESO-FOSMC. The Bouc–Wen

Figure 8. Model validation at f = 50 Hz, solid line: simulation output, dashed line: experimental output.

Table 2. RMS and maximum error of the model deviation.

Frequency (Hz)	Max error (μm)	RMS (μm)
30 Hz	1.1514	0.3806
40 Hz	1.5369	0.4375
50 Hz	1.8117	0.6623
(10,20,30,40,50) Hz	1.7029	0.4719
(5,15,25,35,15) Hz	1.2916	0.4151

RMS: root mean square.

inverse model is connected with the PEA so as to compensate its hysteresis nonlinearity. The compensation error is treated as uncertainties. Furthermore, the ESO-FOSMC is adopted to eliminate or to reduce the influence of the compensation error. The control structure of the system is shown in Figure 11, where x_d is the reference input, N is a Bouc–Wen model, N^{-1} is the inverse Bouc–Wen model which compensates the hysteresis nonlinearity, $G(s)$ is the linear dynamic part, ESO represents the extended state observer, and FOSMC represents the fractional order sliding-mode controller.

Hysteresis compensator

In order to eliminate the hysteresis nonlinearity of the PEA, a static hysteresis compensator is designed, which is to drive the output signal v to track the reference signal v_r, see Figure 12.

Denote $H(\cdot)$ as the hysteretic nonlinear operator described by equation (2b). The Bouc–Wen model and the inverse model (hysteresis compensator) can be written respectively as

$$v = du - H(u) \tag{10}$$

and

$$u = \frac{v_r + H(u)}{d} \tag{11}$$

where the scalar d has been identified, and $d - H(\cdot)$ is invertible in general, c.f. equation (10). Note that the
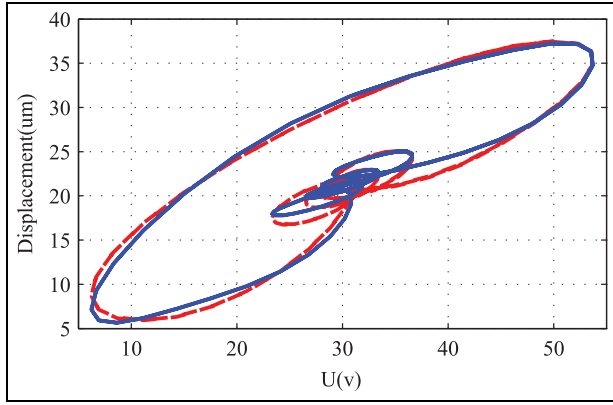
Figure 9. Model validation at $f = (10,\ 20,\ 30,\ 40,\ 50)$ Hz, solid line: simulation output, dashed line: experimental output.
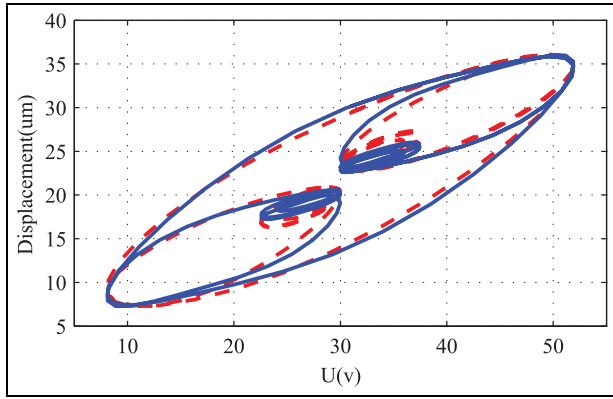

Figure 10. Model validation at $f = (5,\ 15,\ 25,\ 35,\ 45)$ Hz, solid line: simulation output, dashed line: experimental output.
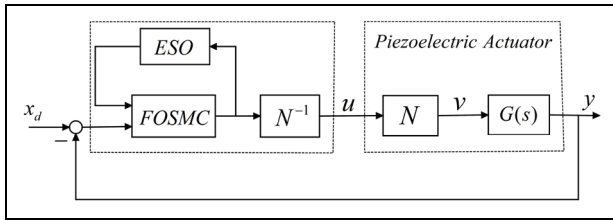

Figure 11. Structure of control system.

hysteresis compensator takes the reference signal v_r as input and the control signal u as output.

Since the hysteresis compensator (11) is a static non-linear term, it can compensate static hysteresis only.[40] The output of the hysteresis compensator and the PEA is symmetric with respect to $y = x$ while the frequency of the input signal is $f = 0.5$ Hz, c.f. Figure 13.

While adopting the hysteresis compensator, the system under consideration can be treated as a linear system with disturbances. Therefore, the SMC and extended state observer can be designed, respectively, due to the separation principle.
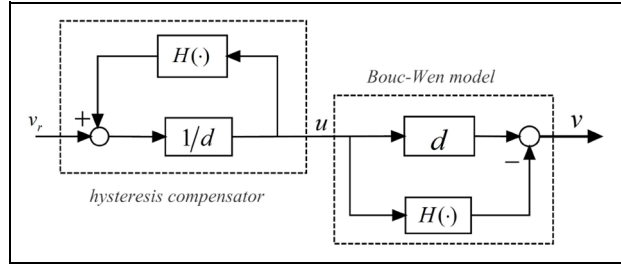

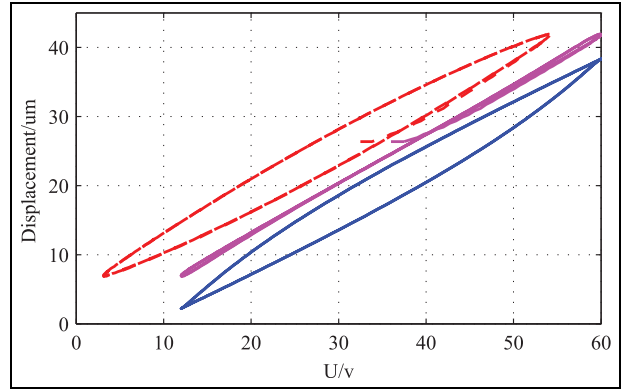**Figure 12.** Structure of hysteresis compensator.

Figure 13. Hysteresis compensation at $f = 0.5$ Hz, solid line: hysteresis compensation output, dashed line: PEA output.

Extended state observer

In this part, an extended state observer is designed to observe external disturbances, model-plant mismatches and unmodeled dynamics.

Suppose that the disturbances φ are acting on the input of the plant $G(s)$, and φ is differentiable with respect to t.

The state-space description of $G(s)$ is

$$\begin{cases} \dot{x}_1 = x_2 \\ \dot{x}_2 = -\frac{k}{m}x_1 - \frac{c}{m}x_2 + \frac{k_1}{m}(v + \varphi) \\ y = x_1 \end{cases} \tag{12}$$

Treat the disturbance of $(k_1/m)\varphi$ as an extended state x_3, that is, $x_3 := \frac{k_1}{m}\varphi$, and rewrite equation (12) as

$$\begin{cases} \dot{x}_1 = x_2 \\ \dot{x}_2 = -\frac{k}{m}x_1 - \frac{c}{m}x_2 + x_3 + \frac{k_1}{m}v \\ \dot{x}_3 = \vartheta \\ y = x_1 \end{cases} \tag{13}$$

where ϑ is the differential of $(k_1/m)\varphi$. Note that the systems equation (13) is observable. Design an extended state observer of the system equation (13) as

$$\begin{cases} \dot{z}_1 = z_2 - \beta_1(\hat{y} - y) \\ \dot{z}_2 = -\frac{k}{m}z_1 - \frac{c}{m}z_2 + \frac{k_1}{m}v + z_3 - \beta_2(\hat{y} - y) \\ \dot{z}_3 = -\beta_3(\hat{y} - y) \\ \hat{y} = z_1 \end{cases} \tag{14}$$

where z_1, z_2, and z_3 are the state of the extended state observer, $\hat{y}$ is the output of the observer, β_1, β_2, and β_3

are the observer gains to be determined. Note that in equation (14), z_1, z_2, and z_3 are the observed values of the state x_1, x_2, and $(k_1/m)\varphi$, respectively. Therefore, the disturbance term $(k_1/m)\varphi$ in equation (12) can be approximated by the state z_3 of the extended state observer.

Denote $\varepsilon_i = x_i - z_i$ for all $i = 1, 2, 3$ and $\varepsilon := [\varepsilon_1 \quad \varepsilon_2 \quad \varepsilon_3]^T$. The dynamics of the error system is

$$\dot{\varepsilon} = A\varepsilon - L(\hat{y} - y) + B_w\vartheta$$
$$= (A - LC)\varepsilon + B_w\vartheta \qquad (15)$$

where

$$A = \begin{bmatrix} 0 & 1 & 0 \\ -\frac{k}{m} & -\frac{c}{m} & 1 \\ 0 & 0 & 0 \end{bmatrix}, \quad L = \begin{bmatrix} \beta_1 \\ \beta_2 \\ \beta_3 \end{bmatrix},$$
$$C = [1 \quad 0 \quad 0], \text{ and } B_w = [0 \quad 0 \quad 1]^T$$

The eigenvalue of the matrix $(A - LC)$ determines the attenuation rate of the observer error, that is, the farther the distance to the imaginary axis, the faster the observation error attenuates. Assign the pole of $(A - LC)$ on the left half plane[41]

$$\lambda_0(s) = |sI - (A - LC)| = (s + w_0)^3 \qquad (16)$$

where w_0 is the bandwidth of the observer. That is, parameters of the extended state observer satisfy the following equation

$$\begin{cases} \beta_1 + \frac{c}{m} = 3w_0 \\ \frac{c}{m}\beta_1 + \beta_2 + \frac{k}{m} = 3w_0^2 \\ \beta_3 = w_0^3 \end{cases} \qquad (17)$$

The error system equation (15) is input-to-state stable with respect to ϑ,[42] while $w_0 > 0$ is on the left half plane. Theoretically, the state of observer is approximated to the actual state of the system at arbitrary fast speed if the disturbance of φ varies slowly, c.f., $\vartheta \approx 0$.

Theorem 1. Assume that ϑ in system equation (13) is bounded, that is, $|\vartheta| \leq M_1$ for a given $M_1 > 0$. Then the estimated error of the extended state observer is bounded, that is, $\|\varepsilon\| \leq M_2$ for some given M_2. Moreover, $\lim_{t\to\infty} \varepsilon(t) = 0$.

Proof. Denote $A_1 = A - LC$. Then

$$\varepsilon(t) = \exp(A_1 t)\varepsilon(0) + \int_0^t \exp(A_1(t-\tau))B_w\vartheta d\tau \qquad (18)$$

and

$$\|\varepsilon(t)\| \leq \|\exp(A_1 t)\| \|\varepsilon(0)\| + \int_0^t \|\exp(A_1(t-\tau))\| \|B_w\| \|\vartheta\| d\tau \qquad (19)$$

where $\|\cdot\|$ is any Euclidean norm.

According to equation (16), A_1 has triple eigenvalues with $\lambda_1 = \lambda_2 = \lambda_3 = -w_0$, then there exists $\kappa > 1$ such that for all $t \geq 0$

$$\|\exp(A_1 t)\| \leq \kappa \exp(-w_0 t) \qquad (20)$$

$$\|\exp(A_1(t-\tau))\| \leq \kappa \exp(-w_0(t-\tau)) \qquad (21)$$

Then equation (19) can be rewritten as

$$\|\varepsilon(t)\| \leq \kappa \exp(-w_0 t)\|\varepsilon(0)\| + \frac{\kappa M_1}{w_0}(1 - \exp(-w_0 t))$$

Denote $M_2 := \kappa \|\varepsilon(0)\| + (\kappa M_1/w_0)$, then $\|\varepsilon(t)\| \leq M_2$ for all $t \geq 0$, and $\lim_{t\to\infty} \varepsilon(t) = 0$.

ESO-SMC

In order to ensure robustness, conventional SMC needs to know the upper bound of disturbances or model uncertainties, although somehow it is impossible in the process of control design. SMC method with a disturbance estimation is proposed[29,30] in which the upper bound of disturbances or model uncertainties is no longer needed.

Denote the displacement error as

$$e = y - x_d = x_1 - x_d \qquad (22)$$

where x_d is the reference input.

Due to $(k_1/m)\varphi - z_3 = \varepsilon_3$, the dynamics of e is

$$\dot{e} = x_2 - \dot{x}_d$$
$$\ddot{e} = \dot{x}_2 - \ddot{x}_d \qquad (23)$$
$$= -\ddot{x}_d - \frac{k}{m}x_1 - \frac{c}{m}x_2 + \frac{k_1}{m}v + z_3 + \varepsilon_3$$

Furthermore, define a sliding surface as

$$s = \lambda e + \dot{e} \qquad (24)$$

where $\lambda > 0$ is a controller parameter that needs to be tuned.

Due to equations (22) and (23), the system dynamics along the sliding surface is

$$\dot{s} = \lambda\dot{e} + \ddot{e}$$
$$= \lambda(x_2 - \dot{x}_d) - \ddot{x}_d - \frac{k}{m}x_1 - \frac{c}{m}x_2 + \frac{k_1}{m}v + z_3 + \varepsilon_3$$

Choose the SMC of v as

$$v = \frac{m}{k_1}\left[\lambda(\dot{x}_d - x_2) + \ddot{x}_d + \frac{k}{m}x_1 + \frac{c}{m}x_2 - \rho s - \eta \, \text{sgn}(s)\right] - \frac{m}{k_1}z_3 \qquad (25)$$

The real control law applying to the system is $u = (v + H(u))/d$ in terms of equation (10), where

$$v = \frac{m}{k_1}\left[\lambda(\dot{x}_d - z_2) + \ddot{x}_d + \frac{k}{m}x_1 + \frac{c}{m}z_2 - \rho s - \eta \, \text{sgn}(s)\right] - \frac{m}{k_1}z_3 \qquad (26)$$

x_1 is a measured displacement and x_2 in equation (25) are replaced by z_2 since x_2 cannot be measured

directly. z_3 is one of the states of the extended state observer, ρ and η are parameters to be determined. Then, the dynamics of systems with the control v along the sliding surface is

$$\dot{s} = -\rho s - \eta \, \mathrm{sgn}(s) + \varepsilon_3 \tag{27}$$

ESO-FOSMC

Fractional calculus is a generalization of the traditional integer calculus to non-integer orders. The operator of fractional calculus is represented by symbol ${}_{t_0}D_t^\sigma$

$$
{}_{t_0}D_t^\sigma \triangleq D^\sigma = \begin{cases} \dfrac{d^\sigma}{dt^\sigma}, & R(\sigma) > 0 \\ 1, & R(\sigma) = 0 \\ \displaystyle\int_{t_0}^{t} (d\tau)^{-\sigma}, & R(\sigma) < 0 \end{cases} \tag{28}
$$

where t_0, t are the upper and lower limits of the calculus operators, $\sigma \in R$ is the order of the operator, $R(\sigma)$ represents the real part of σ.

The most commonly used definition of fractional calculus is the Riemann–Liouville definition

$$
{}_{t_0}D_t^\sigma f(t) = \frac{1}{\Gamma(n-\sigma)} \left(\frac{d}{dt}\right)^n \int_{t_0}^{t} \frac{f(\tau)}{(t-\tau)^{1-(n-\sigma)}} \, d\tau \tag{29}
$$

where n is an interger with $n-1 < \sigma < n$, $\Gamma(\cdot)$ is the Gamma function.

Under the zero initial condition, the Laplace transform of fractional calculus based on Riemann–Liouville definition is

$$
L\{{}_{t_0}D_t^\sigma f(t)\} = s^\sigma F(s) \tag{30}
$$

The function $f(t)$ is difficult to calculate due to the complexity of equation (29). The Oustaloup filtering method[43] can be used to approximate a fractional calculus operator in the specified frequency range of (w_b, w_h), that is

$$
s^\sigma \approx G_f(s) = \tilde{K} \prod_{i=-N}^{N} \frac{s + w'_i}{s + w_i} \tag{31}
$$

where $N = 2$, w'_i, w_i are obtained by

$$
\begin{aligned}
w'_i &= w_b \left(\frac{w_h}{w_b}\right)^{\frac{k+N+\frac{1}{2}(1-\sigma)}{2N+1}} \\
w_i &= w_b \left(\frac{w_h}{w_b}\right)^{\frac{k+N+\frac{1}{2}(1+\sigma)}{2N+1}} \\
\tilde{K} &= w_h{}^\sigma
\end{aligned} \tag{32}
$$

According to the theory of fractional calculus, a fractional sliding surface is designed

$$
s = \lambda e + \dot{e} + c_0 D^{-\sigma} e \tag{33}
$$

where $\lambda > 0$, $c_0 > 0$ are controller parameters, $\sigma \in (0, 1]$ is the fractional order.

Due to equations (22) and (23), the system dynamics along the sliding surface is

$$
\begin{aligned}
\dot{s} &= \lambda \dot{e} + \ddot{e} + c_0 D^{1-\sigma} e \\
&= \lambda(x_2 - \dot{x}_d) - \ddot{x}_d - \frac{k}{m}x_1 - \frac{c}{m}x_2 \\
&\quad + \frac{k_1}{m}v + z_3 + \varepsilon_3 + c_0 D^{1-\sigma}(x_1 - x_d)
\end{aligned} \tag{34}
$$

Choose the fractional order SMC law as

$$
v = \frac{m}{k_1} \left[\begin{matrix} \lambda(\dot{x}_d - x_2) + c_0 D^{1-\sigma}(x_d - x_1) \\ + \ddot{x}_d + \frac{k}{m}x_1 + \frac{c}{m}x_2 - \rho s - \eta \mathrm{sgn}(s) \end{matrix} \right] - \frac{m}{k_1}z_3 \tag{35}
$$

Furthermore, the real control law applying to the system is $u = (v + H(u))/d$ in terms of equation (10), where

$$
v = \frac{m}{k_1} \left[\begin{matrix} \lambda(\dot{x}_d - z_2) + c_0 D^{1-\sigma}(x_d - x_1) + \ddot{x}_d \\ + \frac{k}{m}x_1 + \frac{c}{m}z_2 - \rho s - \eta \mathrm{sgn}(s) \end{matrix} \right] - \frac{m}{k_1}z_3 \tag{36}
$$

x_1 is a measured displacement, and x_2 in equation (36) are replaced by z_2, since x_2 cannot be measured directly. z_3 is one of the states of the extended state observer, ρ and η are parameters to be determined. Then, the dynamics of systems with the control v along the sliding surface is

$$
\dot{s} = -\rho s - \eta \, \mathrm{sgn}(s) + \varepsilon_3 \tag{37}
$$

Remark 1. The sliding surface dynamics of ESO-FOSMC and ESO-SMC are consistent.

Stability analysis

Define a candidate Lyapunov function

$$
V := \frac{1}{2}s^2 \tag{38}
$$

The first-order differential of equation (38) is

$$
\begin{aligned}
\dot{V} &= s[-\rho s - \eta \, \mathrm{sgn}(s) + \varepsilon_3] \\
&\leq -\rho s^2 - \eta|s| + |\varepsilon_3||s| \\
&= -|s|(\rho|s| + \eta - |\varepsilon_3|)
\end{aligned} \tag{39}
$$

To guarantee that $\dot{V} \leq 0$, that is, the system converges to the sliding surface of $s = \lambda e + \dot{e} + c_0 D^{-\sigma} e$ or $s = \lambda e + \dot{e}$, the following condition has to be satisfied

$$
\eta \geq |\varepsilon_3| \tag{40}
$$

Remark 2. Since $\dot{V} \leq 0$ in equation (39) while $\eta \geq |\varepsilon_3|$ is chosen, the system converges to the sliding surface of $s = 0$. Furthermore, due to $s = \lambda e + \dot{e} + c_0 D^{-\sigma} e = 0$, the system state converges to reference signals. Thus, the convergence rate of the proposed control algorithm can be determined by parameters of λ, c_0, σ, ρ, and η due to equations (33) and (39).

An original SMC, that is, without extended state observer, is determined as

$$\tilde{v} = \frac{m}{k_1}\left[\tilde{\lambda}(\dot{x}_d - \tilde{z}_2) + \tilde{c}_0 D^{1-\sigma}(x_d - x_1) + \ddot{x}_d + \frac{k}{m}x_1 \right.$$
$$\left. + \frac{c}{m}\tilde{z}_2 + (-\tilde{\rho}s - \tilde{\eta}\,\mathrm{sgn}(s))\right]$$

$$(41)$$

where $\tilde{\lambda}$, $\tilde{\rho}$, $\tilde{\eta}$, $\tilde{c}_0$ are controller parameters that need to be tuned, and $\tilde{z}_2$ is the state of the corresponding Luenberger observer. With the original SMC, the first-order differential of the candidate Lyapunov function is

$$\dot{V} = s\dot{s}$$
$$= s\left[\tilde{\lambda}(\tilde{z}_2 - \dot{x}_d) + \tilde{c}_0 D^{1-\sigma}(x_1 - x_d) - \ddot{x}_d - \frac{k}{m}x_1 \right.$$
$$\left. - \frac{c}{m}\tilde{z}_2 + \frac{k_1}{m}\tilde{v} + \frac{k_1}{m}\varphi\right]$$

$$(42)$$

Due to equation (41), equation (42) can be written as follows

$$\dot{V} = s\left[-\tilde{\rho}s - \tilde{\eta}\,\mathrm{sgn}(s) + \frac{k_1}{m}\varphi\right]$$
$$\leqslant -\tilde{\rho}s^2 - \tilde{\eta}|s| + \frac{k_1}{m}\varphi|s|$$

Accordingly, to guarantee $\dot{V} \leqslant 0$, the following condition has to be satisfied

$$\tilde{\eta} \geqslant \frac{k_1}{m}|\varphi| \qquad (43)$$

Comparing equation (43) with (40), the uncertainties are transformed from $(k_1/m)\varphi$ to ε_3 due to the use of the extended state observer where in general $|\varepsilon_3| \ll (k_1/m)|\varphi|$. Thus, on account of the introduction of extended state observer, the parameter of η can be chosen much smaller.

Remark 3. According to the previously identified parameters of k_1 and m, the value of $\tilde{\eta}$ is relatively large, which is not allowed by the experimental equipment.

Remark 4. To alleviate chattering phenomenon, the sign function $sgn(s)$ is replaced by the smooth function[44]

$$con(s) = \frac{s}{|s| + \delta} \qquad (44)$$

for all $\delta > 0$.

Real-time tracking control experiment

In order to verify the effectiveness of the designed ESO-FOSMC, a physical experiment is carried out. The parameters of the controller are listed in Table 3.

Table 3. Controller parameter settings.

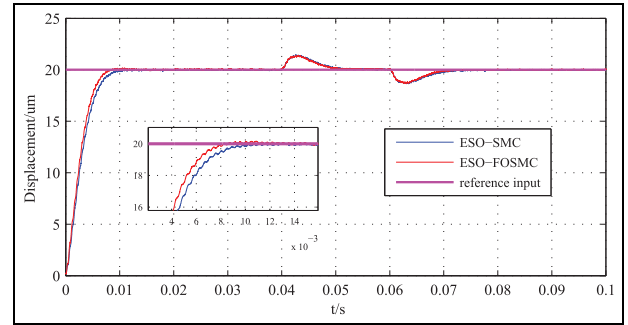| Parameters	Value
λ	800
c_0	1200
σ	0.2
η	0.5
ρ	600
w_0	2100
δ	3

Figure 14. Experimental result of external disturbance rejection and step response.

External disturbance rejection and step responses

Choose a reference signal $x_d = 20$ μm for all $t \geqslant 0$, that is, the frequency of $f = 0$ Hz. Consider an external disturbance

$$\varphi = \begin{cases} 0.5\,\mathrm{V} & t \in [0.04,\ 0.06] \\ 0 & \text{otherwise} \end{cases}$$

That is, an external disturbance of amplitude 0.5 V for 0.02-s duration is added to the PEA. Figure 14 shows the tracking trajectories with the ESO-FOSMC where the proposed ESO-FOSMC can eliminate or attenuate the influence of the disturbances. The experimental results also show that the proposed ESO-FOSMC strategy has faster response time compared with ESO-SMC.

Sinusoidal signal tracking experiment

Choose a single frequency input signal

$$x_d = 20\sin(2\pi ft - \pi/2) + 20\ \mu\mathrm{m}$$

where $f = 10, 20, 30, 40$, and 50 Hz, respectively. The evolutions of displacement and error of the PEA are shown in Figures 15–19, accordingly.

Then choose two composite input signals

$$x_d = 5(5 - cos(2\pi f_1 t) - \cdots - cos(2\pi f_5 t))\ \mu\mathrm{m}$$

where $f_1 = 10$ Hz, $f_2 = 20$ Hz, $f_3 = 30$ Hz, $f_4 = 40$ Hz, $f_5 = 50$ Hz in the first compounding frequency input signal and $f_1 = 5$ Hz $f_2 = 15$ Hz, $f_3 = 25$ Hz,
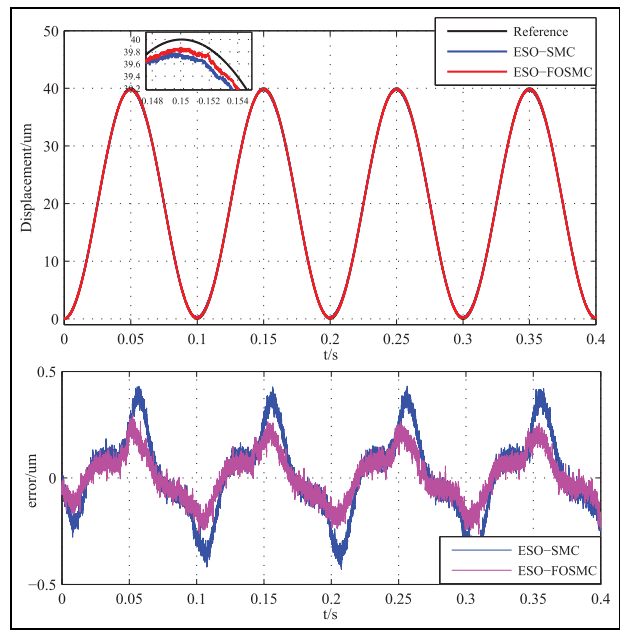
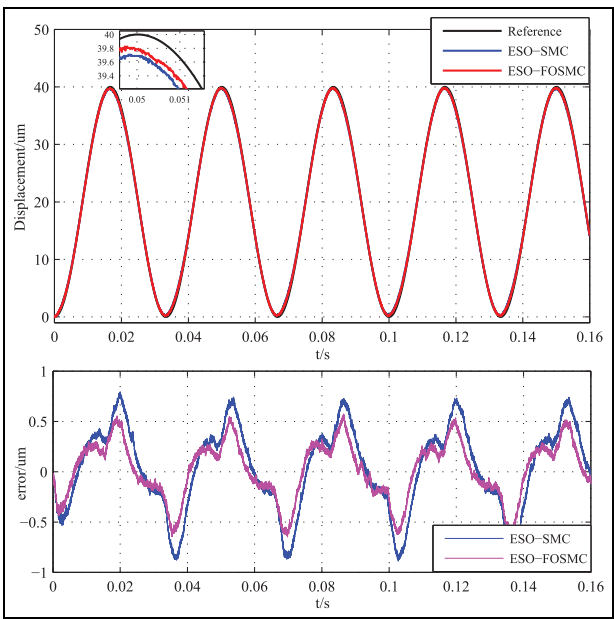**Figure 15.** Trajectory tracking results (f = 10 Hz).

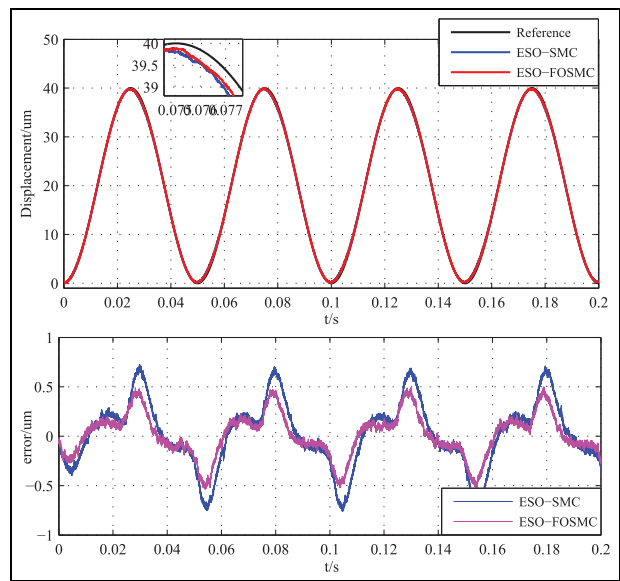**Figure 17.** Trajectory tracking results (f = 30 Hz).

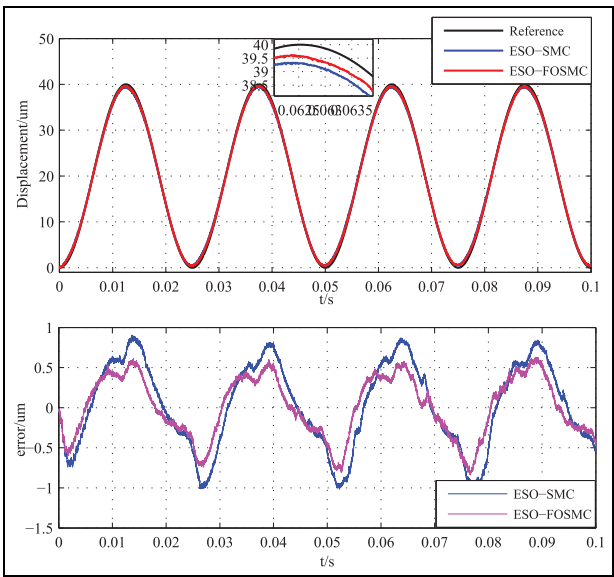**Figure 16.** Trajectory tracking results (f = 20 Hz).

Figure 18. Trajectory tracking results (f = 40 Hz).

Table 4. RMS and maximum error.

Reference input frequency (Hz)	ESO-SMCRMS (μm)	ESO-SMCMax error (μm)	ESO-FOSMCRMS (μm)	ESO-FOSMCMax error (μm)
10	0.1856	0.4304	0.1099	0.2992
20	0.3296	0.7244	0.2167	0.4991
30	0.4210	0.7922	0.2855	0.5738
40	0.5329	0.9027	0.3797	0.6279
50	0.7177	1.2829	0.5329	0.9060
(10,20,30,40,50)	0.3509	0.7725	0.2430	0.5454
(5,15,25,35,45)	0.3385	0.7611	0.2271	0.5588

RMS: root mean square; ESO-SMC: extended state observer–based conventional sliding-mode controller; ESO-FOMSC: extended state observer–based fractional order sliding-mode control.
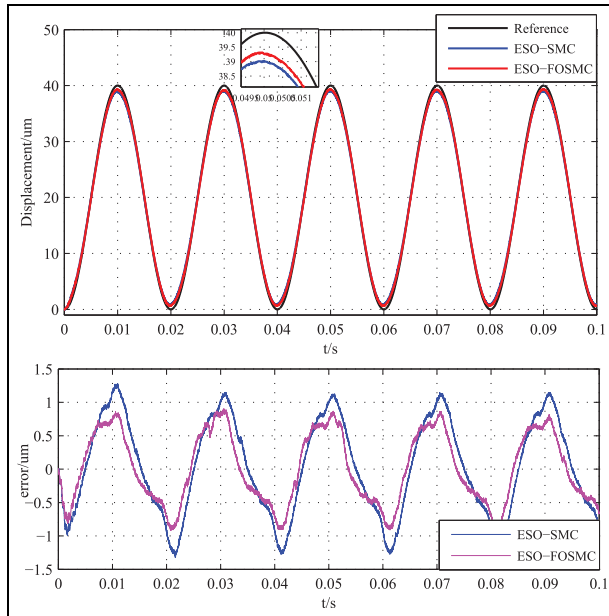
Figure 19. Trajectory tracking results (f = 50 Hz).
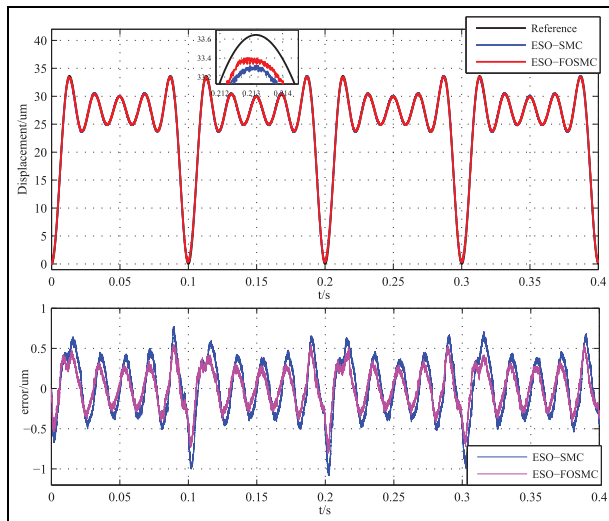

Figure 20. Trajectory tracking results (f = 10, 20, 30, 40, 50 Hz).

$f_4 = 35$ Hz, $f_5 = 45$ Hz in the second compounding frequency input signal. The evolutions of displacement and the error of PEAs are shown accordingly in Figures 20 and 21. Both the RMS error and the maximum error of the trajectory tracking at different frequency are listed in Table 4.

The experiment results above indicate that the PEA can track both single-frequency signals and composite signals in a relatively large-frequency range, that is, the maximum relative error is within 2.5%. In particular, at low frequencies, for example, $f \leqslant 20$ Hz, the relative error is less than 1.25%, which demonstrates the effectiveness of the control scheme. The experimental results also show that the proposed ESO-FOSMC strategy has
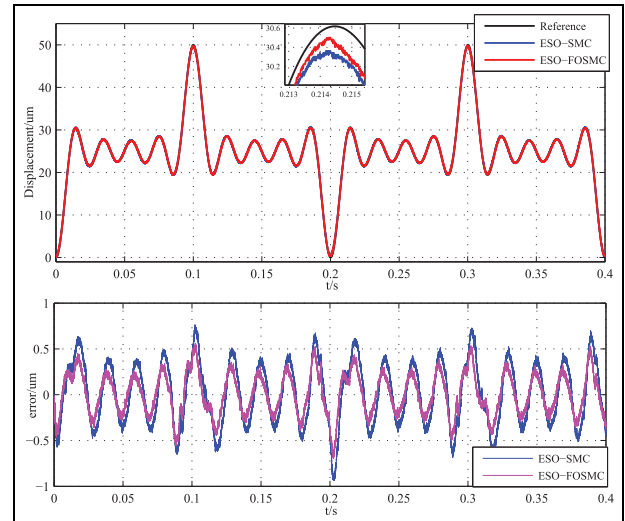

Figure 21. Trajectory tracking results (f = 5, 15, 25, 35, 45 Hz).

smaller tracking error compared with ESO-SMC. Note that the relative error and frequency range that can be tracked are determined by both the controller and the physical limitation.

Conclusion

In order to describe hysteresis nonlinearity of PEAs, a Hammerstein rate-dependent hysteresis model was established and validated using the experimental data in this article. In the controller design process, an inverse Bouc–Wen model was connected in series with the PEA to compensate the hysteresis nonlinearity. ESO-FOSMC was designed to reduce the influence of the incomplete compensation, model-plant mismatches at high-frequency and external disturbances. Moreover, the bounds of the estimation error for extended state observer are estimated, and the convergence of the proposed control strategy is proved. The experimental results showed that PEAs with the proposed controller has faster response time and smaller tracking error in tracking a reference signal over a range of frequency, compared with ESO-SMC. The future work will focus on an adaptive fractional order SMC which can tune the controller parameters online.

ORCID iD

Shuyou Yu https://orcid.org/0000-0002-3258-6494

References

1. Vorbringer-Dorozhovets N, Hausotte T, Manske E, et al. Novel control scheme for a high-speed metrological scanning probe microscope. *Meas Sci Technol* 2011; 22(9): 13.
2. Woody S and Smith S. Design and performance of a dual drive system for tip-tilt angular control of a 300 mm diameter mirror. *Mechatronics* 2006; 16(7): 389–397.
3. Hagood NW, Chung WH and Von Flotow A. Modelling of piezoelectric actuator dynamics for active structural control. *J Intel Mat Syst Str* 1990; 1(3): 327–354.
4. Meldrum DR. A biomechatronic fluid sample handling system for DNA processing. *IEEE/ASME T Mech* 2002; 2(2): 99–109.
5. Guo Y, Zhang Z and Mao J. Rate-dependent Hammerstein model and robust tracking control of giant magnetostrictive actuators. *Acta Automat Sin* 2014; 40(2): 197–207.
6. Goldfarb M and Celanovic N. A lumped parameter electromechanical model for describing the nonlinear behavior of piezoelectric actuators. *J Dyn Syst: T ASME* 1997; 119(3): 478–485.
7. Lin CJ and Lin PT. Tracking control of a biaxial piezo-actuated positioning stage using generalized Duhem model. *Comput Math Appl* 2012; 64(5): 766–787.
8. Jiles DC and Atherton DL. Theory of ferromagnetic hysteresis. *J Magn Magn Mater* 1984; 55(6): 2115–2120.
9. Qin YX and Hu DJ. Nonlinear modeling for piezoelectric actuators. *J Shanghai Jiaotong Univ* 2004; 38(8): 1334–1336.
10. Ge P and Jouaneh M. Generalized preisach model for hysteresis nonlinearity of piezoceramic actuators. *Precis Eng* 1997; 20(2): 99–111.
11. Gu GY, Zhu LM and Su CY. Modeling and compensation of asymmetric hysteresis nonlinearity for piezoceramic actuators with a modified Prandtl–Ishlinskii model. *IEEE T Ind Electron* 2014; 61(3): 1583–1595.
12. Ye M and Wang X. Parameter estimation of the Bouc Wen hysteresis model using particle swarm optimization. *Smart Mater Struct* 2007; 16(16): 2341–2349.
13. Charalampakis AE and Dimou CK. Identification of Bouc-Wen hysteretic systems using particle swarm optimization. *Comput Struct* 2010; 88(21–22): 1197–1205.
14. Dong R, Tan Y, Chen H, et al. A neural network based model for rate-dependent hysteresis for piezoceramic actuators. *Sensor Actuator* 2008; 143(2): 370–376.
15. Wong PK, Xu Q, Vong CM, et al. Rate-dependent hysteresis modeling and control of a piezostage using online support vector machine and relevance vector machine. *IEEE T Ind Electron* 2012; 59(4): 1988–2001.
16. Croft D, Shedd G and Devasia S. Creep, hysteresis, and vibration compensation for piezoactuators: atomic force microscopy application. *Amer Contr Conf* 2001; 3(1): 2123–2128.
17. Ge P and Jouaneh M. Tracking control of a piezoceramic actuator. *IEEE T Contr Syst T* 1996; 4(3): 209–216.
18. Wang ZY, Zhen Z and Zhou KM. Dynamic hysteresis modeling and H-infinity robust control of piezoelectric actuators. *IEE P: Contr Theor Ap* 2014; 31(1): 35–41.
19. Liu P, Wang ZY, Zhang Z, et al. Modeling and robust control of a smart structure with rate-dependent hysteresis nonlinearity. *Int J Automat Comput* 2014; 11(1): 51–58.
20. Wang Y, Zhou W, Luo J, et al. Reliable intelligent path following control for a robotic airship against sensor faults. *IEEE/ASME T Mech* 2019; 24(6): 2572–2582.
21. Wang Y, Karimi HR, Shen H, et al. Fuzzy-model based sliding mode control of nonlinear descriptor systems. *IEEE T Cybernetics* 2019; 49(9): 3409–3419.
22. Jiang B, Karimi HR, Kao Y, et al. Adaptive control of nonlinear semi-Markovian jump T-S fuzzy systems with immeasurable premise variables via sliding mode observer. *IEEE T Cybernetics* 2018; 50(2): 810–820.
23. Jiang B, Karimi HR, Kao Y, et al. Takagi-Sugeno model-based sliding mode observer design for finite-time synthesis of semi-Markovian jump systems. *IEEE T Syst Man Cyb* 2019; 49(7): 1505–1515.
24. Al-Ghanimi A, Zheng J and Man Z. A fast non-singular terminal sliding mode control based on perturbation estimation for piezoelectric actuators systems. *Int J Control* 2017; 90(3): 496–507.
25. Li ZC, Zheng S, Wang HN, et al. Fractional order sliding mode control for nano-positioning of piezoelectric actuator. In: *The 31st Chinese control and decision conference*, Nanchang, China, 3–5 June 2019. New York: IEEE.
26. Xue H, Shao ZP, Pan JC, et al. Fractional-order dual-loop adaptive terminal sliding mode control for dynamic positioning. *IEE P: Contr Theor Ap* 2019; 36(10): 1745–1754.
27. Dumlu A. Design of a fractional-order adaptive integral sliding mode controller for the trajectory tracking control of robot manipulators. *Proc IMechE, Part I: J Systems and Control Engineering* 2018; 232(9): 1212–1229.
28. Ayten KK, Ciplak MH and Dumlu A. Implementation a fractional-order adaptive model-based PID-type sliding mode speed control for wheeled mobile robot. *Proc IMechE, Part I: J Systems and Control Engineering* 2019; 233(8): 1067–1084.
29. Elmali H and Olgac N. Sliding mode control with perturbation estimation (SMCPE): a new approach. *Int J Control* 1992; 56(4): 923–941.
30. Elmali H and Olgac N. Implementation of sliding mode control with perturbation estimation (SMCPE). *IEEE T Contr Syst T* 1996; 4(1): 79–85.
31. Bashash S and Jalili N. Robust multiple frequency trajectory tracking control of piezoelectrically driven micro/nanopositioning systems. *IEEE T Contr Syst T* 2007; 15(5): 867–878.
32. Yang L and Li J. Robust output feedback control with disturbance estimation for piezoelectric actuators. *Neurocomputing* 2016; 173: 2129–2135.
33. Li Y and Xu Q. Adaptive sliding mode control with perturbation estimation and PID sliding surface for motion tracking of a piezo-driven micromanipulator. *IEEE T Contr Syst T* 2010; 18(4): 798–810.
34. Tsai MS and Chen JS. Robust tracking control of a piezoactuator using a new approximate hysteresis model. *J Dyn Syst: T ASME* 2003; 125(1): 96–102.
35. Sofla MS, Rezaei SM, Zareinejad M, et al. Hysteresis-observer based robust tracking control of piezoelectric actuators. *Amer Contr Conf* 2010; 58(8): 4187–4192.

36. Sofla MS, Barazandeh F, Rezaei SM, et al. Observer-based robust motion control of a piezo-actuated stage under external disturbances. *T I Meas Control* 2012; 34(4): 365–375.

37. Eskinat E, Johnson SH and Luyben WL. Use of Hammerstein models in identification of nonlinear systems. *AIChE J* 1991; 37(2): 255–268.

38. Jia L and Li X-L. Identification of Hammerstein model: review and prospect. *IEE P: Contr Theor Ap* 2014; 31(1): 1–10.

39. Kennedy J and Eberhart R. Particle swarm optimization. *IEEE IJCNN* 1995; 4(8): 1942–1948.

40. Rakotondrabe M. Bouc-Wen modeling and inverse multiplicative structure to compensate hysteresis nonlinearity in piezoelectric actuators. *IEEE T Autom Sci Eng* 2011; 8(2): 428–431.

41. Zheng Q, Gao LQ and Gao Z. On estimation of plant dynamics and disturbance from input-output data in real time. *IEEE Intl Conf Contr* 2007; 254(2): 1167–1172.

42. Khalil HL. *Nonlinear systems*. 3rd ed. Upper Saddle River, NJ: Prentice Hall, 2002.

43. Tepljakov A, Petlenkov E and Belikov J. FOMCON: fractional-order modeling and control toolbox for MATLAB. In: *Proceedings of the 18th international conference mixed design of integrated circuits and systems (MIXDES 2011)*, Gliwice, 16–18 June 2011. New York: IEEE.

44. Chen SM, Hwang RY and Tomizuka M. A state-dependent boundary layer design for sliding mode control. *IEEE T Automat Contr* 2002; 47(10): 1677–1681.